Impact of Preparation Method and Hydrothermal Aging on Particle Size Distribution of Pt/γ-Al_2O_3 and its Performance in CO- and NO-oxidation

E. Ogel[1], M. Casapu[1], D. E. Doronkin[1], R. Popescu[2], H. Störmer[2], C. Mechler[3], G. Marzun[3], S. Barcikowski[3], M. Türk[4], J.-D. Grunwaldt[1*].*

[1]Institute for Chemical Technology and Polymer Chemistry, Karlsruhe Institute of Technology (KIT), 76131 Karlsruhe, Germany

[2]Laboratory for Electron Microscopy, Karlsruhe Institute of Technology (KIT), 76131 Karlsruhe, Germany

[3]Technical Chemistry I and Center for Nanointegration Duisburg-Essen (CENIDE), University Duisburg-Essen (UDE), 45141 Essen, Germany

[4]Institute for Technical Thermodynamics and Refrigeration, Karlsruhe Institute of Technology (KIT), 76131 Karlsruhe, Germany

* Corresponding authors:

Prof. Jan-Dierk Grunwaldt, e-mail: grunwaldt@kit.edu

Dr. Maria Casapu, e-mail: maria.casapu@kit.edu

Abstract

The influence of the preparation method and the corresponding particle size distribution on hydrothermal deactivation behavior at 600-800°C and its performance during CO/NO oxidation was systematically investigated for a series of Pt/Al_2O_3 catalysts. Representative conventional (incipient wetness impregnation) and advanced preparation methods (flame spray pyrolysis, supercritical fluid reactive deposition and laser ablation in liquid) were selected, which generated samples containing narrow and homogeneous but also heterogeneous particle size distributions. Basic characterization was conducted by inductively coupled plasma-optical emission spectrometry, N_2 physisorption and X-ray diffraction. The particle size distribution and the corresponding oxidation state was analyzed using transmission electron microscopy and X-ray absorption spectroscopy. The systematic study shows that oxidized Pt nanoparticles smaller than 2 nm sinter very fast, already at 600°C, but potential chlorine traces from the catalyst precursor seem to stabilize Pt nanoparticles against further sintering and consequently maintain the catalytic performance. Samples prepared by flame spray pyrolysis and laser ablation showed a superior hydrothermal resistance of the alumina support, although, due to small inter-particle distance in case of laser synthesized particles, the particle size distribution increases considerably at high temperatures. Significant deceleration of the noble metal sintering process was obtained for the catalysts containing homogeneously distributed but slightly larger Pt nanoparticles (supercritical fluid reactive deposition) or for particles deposited on a thermally stable alumina support (flame spray pyrolysis). The correlations obtained between Pt particle size distribution, oxidation state and catalytic performance indicate different trends for CO and NO oxidation reactions, in line with structure sensitivity.

1 Introduction

Considering the high costs of the noble metal components in exhaust gas aftertreatment catalysts, numerous efforts have been reported to further improve the efficiency and thermal stability of such catalysts by careful tuning of the preparation methods[1-3]. Generally, the aim is to obtain homogeneously distributed small noble metal nanoparticles, which maximizes the number of the surface active sites and, hence, the efficient use of the noble metals. Nonetheless, large differences in activity are encountered if the shape or the size of the noble metal nanoparticles is varied within the 1-5 nm range[4-9]. This is due to pronounced changes in the redox behavior and binding energies of the reactants and products[9-11]. For Pt/Al_2O_3 catalysts significant differences in the CO, NO and C_3H_6 oxidation activity have been reported if the Pt particle size or shape was varied[4-5, 12-15]. An optimal particle size in the 2-3 nm range was proposed to obtain highly active catalysts for CO oxidation[14, 16] whereas slightly larger particles are necessary to efficiently convert NO to NO_2 [5]. Additionally, reduced Pt sites seem to represent the active species for such oxidation reactions[11, 16]. However, considering the reaction conditions present in a typical exhaust pipe, the durability of such idealized catalysts becomes very important. Particularly, the very small nanoparticles/clusters are expected to be highly mobile, which leads to a rapid drop in dispersion, whereas larger particles require higher temperatures for severe sintering[17-23]. In this regard, the hydrothermal sintering of the noble metal and of the supporting material represent a major problem for the exhaust gas aftertreatment catalysts[17, 24]. To overcome this challenge, typically supports which are able to maintain high noble metal dispersion at elevated temperatures (e.g. CeO_2-ZrO_2) or alloying of Pt with Pd are considered. Nevertheless, also in this case tuning the monometallic or bimetallic noble metal particle dispersion, size and shape, and understanding structure-activity-durability correlations are equally important.

With the present study, we aim at: (1) obtaining a fundamental understanding of the hydrothermal aging behavior of a Pt/Al_2O_3 catalysts series containing noble metal particles with a well-

defined size distribution and (2) correlating the particle growth and variation in noble metal oxidation state after aging at different temperatures with the catalytic activity for CO and NO oxidation. By exploiting different conventional and modern preparation methods we systematically prepared catalysts classes with a homogeneous and narrow Pt particle size distribution (PSD) in the size range of 1-2 nm or 2-4 nm and heterogeneous, polydisperse PSD containing small but also large Pt nanoparticles were investigated. The conventional incipient wetness impregnation (IWI) with different Pt precursors was applied alongside with flame spray pyrolysis (FSP), supercritical fluid reactive deposition (SFRD) and pulsed laser ablation in liquid (PLAL). FSP is a one-step synthesis technique for preparation of high surface area and highly dispersed supported Pt nanoparticles[25]. Materials derived by SFRD of noble metal precursors in CO_2 typically show a narrow particle size distribution and a high dispersion of the metal particles[26-27]. Finally, the preparation of Pt-based catalysts by PLAL[28-29] is a relatively fast method that enables the gram-per-hour-scale[29] synthesis of surfactant-free nanoparticles followed by a particle adsorption on supports by electrostatic interactions controlled by pH [28, 30]. Hence, by employing different preparation techniques the focus of our investigations was laid on uncovering their impact on the particle size distribution and the homogeneity of their lateral dispersion on the support in a fresh Pt-catalyst and particularly their fingerprint on the catalyst evolution during aging. Particularly the first stage of the sintering process, which is more impacted by differences in particle size [20], was investigated. Combining systematic catalyst aging with in-depth characterization and testing, several interesting correlations regarding the size-dependent durability and reactivity were obtained.

2 Experimental Section

2.1 Catalyst preparation

For this study, a series of model DOC ($Pt/\gamma\text{-}Al_2O_3$) catalyst samples with ~ 2 wt.% Pt loading were used. The catalysts were synthesized via the following preparation methods:

Incipient wetness impregnation (IWI): A commercially available large surface area alumina (Puralox SCFA-230 from Sasol) was pre-calcined at 700 °C for 5 h in static air before using it as support material. In order to investigate the effect of different precursors on the particle size distribution, two IWI samples were prepared by using either chloroplatinic acid (HCP) or platinum(II) acetylacetonate (PAA). In case of the chloroplatinic acid ($H_2PtCl_6 \cdot H_2O$) precursor an aqueous solution was used for the impregnation of the $\gamma\text{-}Al_2O_3$ carrier as reported in ref.[16]. For the second sample, the PAA precursor was dissolved in acetone and added to the $\gamma\text{-}Al_2O_3$ carrier. After impregnation, the resulting powders were dried at 80 °C for 12 h and calcined in static air at 500 °C for 5 h.

Flame spray pyrolysis (FSP): For the sample prepared by single nozzle flame spray pyrolysis, in accordance with procedure given in ref.[31] and based on the setup proposed by Mädler et al.[32], the precursor solutions were prepared by dissolving appropriate amount of Pt(II) acetylacetonate (98%, Strem chemicals) in 50 ml toluene and aluminium(III) acetylacetonate in a mixture of acetic acid and methanol (25 ml : 25 ml). Afterwards the carrier and the noble metal solutions were mixed, fed in a capillary tube at 5 ml/min by a syringe pump (World Precision Instruments) and dispersed by a small annular nozzle located at the outlet of the capillary supplying an O_2 flow of 5.0 L min^{-1} at 3 bar pressure drop. The spray was ignited by a premixed CH_4 flame (flame conditions: 1.6 L min^{-1} O_2 and 750 mL min^{-1} CH_4). The gas flows were adjusted by MKS mass flow controllers. The produced catalyst particles were collected on glass fiber filters (75 cm diameter, Whatman GF6) in a water-cooled round holder connected to a vacuum pump (Busch R5). The obtained catalyst powder (~0.8 g) was calcined at 500 °C for

5 h in air in order to remove organic residues of the precursor solution, which were indicated to be released between 350-450°C during a thermal analysis experiment on a STA 449 F3 Jupiter unit (Netzsch).

Supercritical fluid reactive deposition (SFRD): For the SFRD [33-36] preparation procedure certain amounts of the (1,5-cyclooctadiene)dimethyl platinum(II) precursor and γ-Al_2O_3 substrate (Puralox SCFA-230 from Sasol, the same as used for IWI) were filled in two separate open vessels which were placed in a stainless steel reactor (V = 49 cm^3). The system is equipped with a magnetic stirrer for improved mixing of the supercritical solution. After evacuation, the system was treated in supercritical CO_2 (sc-CO_2) at 15.5 MPa and 353 K for 20 h. Thereby the dissolved precursor is adsorbed on the substrate. In the next step, H_2 was added to the system and the mixture was kept for additional 2 h at isothermal and isobaric conditions in order to convert the metallic precursor into its metal form. Finally, the system was slowly depressurized and cooled down to ambient conditions.

Pulsed laser ablation in liquid (PLAL): Similar to earlier nanoparticle synthesis by PLAL[28, 37] the colloid production was conducted using a Nd:YAG laser (Ekspla, Atlantic) with a pulse duration of 10 ps, a repetition rate of 100 kHz, and a laser wavelength of 1064 nm. Thereby, the Pt target is ablated in aqueous solutions of 0.1 mmol/L sodium carbonate buffer (Na_2CO_3, Merck 99.5 % and $NaHCO_3$, Fluka 99.0 %) with a pH of 9.9. The ablated mass was determined by gravimetric measurement of the target before and after laser ablation, resulting in Pt mass concentration of 105 μg mL^{-1}. For a size reduction, the colloids were re-irradiated (fragmentation) using an Nd:YAG laser (Edgewave) with a pulse length of 6 ns, a repetition rate of 3 kHz, and a laser wavelength of 532 nm. To cut-off particle diameters or aggregates > 10 nm, a subsequent centrifugation step is carried out with a centrifuge from Hettich (Universal 320, 5000 rpm)[30]. The ligand-free Pt NP`s were used for colloidal deposition on alumina in a batch mode.

For simplicity, the following acronyms will be used for referring to the differently prepared fresh catalysts (calcined at 500°C): “HCP-500” and “PAA-500” for the catalysts obtained by incipient wetness impregnation with hexachloroplatinic acid and platinum (II) acetylacetonate precursors, respectively; “FSP-500” for flame made catalyst and “SC-500” for the sample prepared by SFRD; “LA” for catalyst prepared by laser ablation method.

Hydrothermal aging

All catalysts were aged for 5 h in a gas mixture of 2 L min^{-1} containing 10 vol.%. H_2O, 10 vol.% O_2 in N_2 at 600, 700 and 800 °C. Sample codes are used throughout the paper implying preparation method as well as aging temperature, e. g “HCP-800” refers to the catalyst prepared by incipient wetness impregnation with hexachloroplatinic acid and aged at 800°C,” SC-800” refers to the sample prepared by supercritical fluid reactive deposition and aged at 800°C. A full list of the fresh and aged samples is given in the electronic support information (Table S1).

2.2 Catalyst characterization

The Pt/γ-Al_2O_3 powder catalysts were thoroughly characterized by elemental analysis (ICP-OES), N_2 physisorption (BET), X-ray diffraction (XRD), transmission electron microscopy (TEM) and *ex-situ* X-ray absorption spectroscopy (XAS).

The Pt content of the prepared catalysts was determined by using inductively coupled plasma with optical emission spectroscopy (ICP-OES) on an OPTIMA 4300 DV spectrometer (Perkin Elmer).

A Belsorp Mini II (Bel Japan Inc.) was used to measure the BET surface area and the pore volume. In the general pretreatment, all samples were degassed at 300 °C for 2 h. The micropore volume was determined using the t-plot method.

X-ray diffraction (XRD) measurements were performed employing a Bruker D8 Advance diffractometer using Cu-K_α radiation (λ = 1.54 Å). The intensity of scattered X-rays was measured in a 2θ-range of 20-80° with a step size of 0.016° and an acquisition time of 0.51 s per point.

X-ray absorption spectroscopy (XANES and EXAFS) data were acquired at the Pt L_3 edge (11564 eV) at the P64 beamline[38] at PETRA III (Hamburg, Germany) and at the CAT-ACT beamline at the KIT synchrotron[39] (Karlsruhe, Germany). The catalyst samples, platinum oxide and foil references were measured in transmission mode. The analysis of the X-ray absorption near edge structure (XANES) and the extended X-ray absorption fine structure (EXAFS) was performed using the Athena software from the IFFEFIT package[40]. The average Pt oxidation state was determined by a linear combination analysis of the X-ray absorption near edge structure (XANES) spectra using Pt foil and PtO_2 as reference spectra in a fitting range of 11554-11604 eV. The structure refinement was performed basing on the EXAFS spectra with the ARTEMIS software[40]. The k^1-, k^2-, and k^3-weighted EXAFS functions were Fourier transformed in the k range of 3.0–14 $Å^{-1}$ (Hanning window with sills size of 1 $Å^{-1}$). The structural models were based on a Pt metal core (ICSD collection code 64923) and an oxide shell from PtO_2 (ICSD collection code 4415). The corresponding theoretical backscattering amplitudes and phases were calculated by FEFF 6.0 and then adjusted to the experimental spectra by a least square method in R-space between 1 and 3 Å. First, the amplitude reduction factor (S_0^2 = 0.86 at PETRA P64 and S_0^2 = 0.79 at CAT-ACT) was calculated using the spectrum of Pt foil and then the coordination numbers, interatomic distances, energy shift (δE_0) and mean square deviation of interatomic distances (σ^2) were refined. The absolute misfit between theory and experiment was expressed by ρ.

Scanning transmission electron microscopy (STEM) characterization in the high-angle annular dark-field (HAADF) mode was performed using a FEI OSIRIS ChemiSTEM microscope operated at 200 kV or a FEI Titan^3 80-300 aberration-corrected electron microscope operated at

300 kV. For the STEM sample preparation small sample amounts were dispersed in deionized water and drop-casted onto a commercial 400 μm mesh Cu-grid (Plano 01824) covered by a holey amorphous carbon film, with a nominal thickness of 3 nm. The particle size distribution was determined with the help of the ImageJ software[41] based on counting/marking all particles (100-1800 Pt NP) present on a set of micrographs. For the evaluation of NP diameters, the projected area A_i of NPs on HAADF STEM images was measured. The measured areas are evaluated by calculating the particle diameter D_i of the circular projection area of the same size by using the relation:

$$A_i = \pi {D_i}^2/4 \qquad (1)$$

Assuming a spherical shape, the number-averaged particle size D_m and surface-averaged particle size D_s for each distribution were calculated according to[42]:

$$D_m = \frac{\sum_i N_i D_i}{\sum_i N_i} \qquad (2)$$

and

$$D_s = \frac{\sum_i N_i D_i^3}{\sum_i N_i D_i^2} \qquad (3)$$

with N_i = number of particle of size D_i.

2.3 Catalytic tests

Catalytic activity tests with respect to CO and NO oxidation were performed in a continuous-flow fixed-bed quartz reactor (inner diameter 8 mm, outer diameter 10 mm) for the fresh and aged catalysts. A sieve fraction of 125-250 μm was prepared by pressing the powder into a pellet at 5 tons, crushing and sieving. The reactor was loaded with the amount of catalyst corresponding to 1 mg Pt (according to the ICP-OES results on Pt content for each Pt/γ-Al_2O_3 sample) that was mixed with 950 mg quartz sand (150-250 μm), resulting in a catalyst bed of 15 mm fixed between two quartz-wool plugs in the middle of reactor. The temperature was

measured with two thermocouples located at the upstream and downstream side of the catalyst bed. The inlet gas flow composition consisted of 1000 ppm CO/NO and 10 vol.% O_2 in N_2 and was controlled by mass flow controllers supplied by Bronkhorst. A total flow of 500 mL min^{-1} was used, corresponding to a space velocity of 60,000 h^{-1}. Gas concentrations were determined using a Fourier transform infrared spectrometer (FTIR) from MKS (Multigas 2030). The temperature during CO oxidation was increased and then decreased at a controlled rate of 5 °C/min from 50 to 350 °C, describing one cycle. In case of NO oxidation, the temperature range was between 50 and 500 °C. The cycle was repeated three times in order to assess the reproducibility of the results, as well as the aging and stability of each catalyst. However, since the second and third cycles were completely overlapping, in the following we will report only the third light-off/light-out cycle. CO conversion was determined by using the following equation:

$$\mathrm{X(CO)} = (1 - \left(\frac{[\mathrm{CO}]_{\mathrm{out}}}{[\mathrm{CO}]_{\mathrm{in}}}\right)) \cdot 100\ \% \qquad (4)$$

where $[\mathrm{CO}]_{\mathrm{out}}$ and $[\mathrm{CO}]_{\mathrm{in}}$ denote CO concentration at the inlet and outlet of the reactor. NO conversion to NO_2 was calculated in the same way as CO conversion.

3 Results and discussion

3.1 Physical and chemical properties of the as prepared and aged catalysts

3.1.1 Pt content, specific surface area and morphology

Table 1 presents the Pt content obtained by elemental analysis, which with small variations is about 2 wt.% for all samples. The only exception is the sample prepared by laser ablation which contains only 1.2 wt.% Pt. The BET surface areas for the catalysts prepared by the commonly used impregnation technique and by SFRD (Table 1) are quite similar (~160 m^2g^{-1}) due to the use of the same γ-Al_2O_3 carrier. However, the laser generated catalyst has an initial surface area of 183 m^2g^{-1}, which is probably caused by a slight alteration of the morphology that occurred during Pt deposition at a pH of ~3. Slight dissolution in water of small alumina nanoparticles due to pH variation has been reported before[43-44], with the reformation of smaller grains during catalyst calcination at 500°C. Analog, and as expected for such materials[45], the flame made catalyst has a significantly higher surface area amounting to 220 m^2g^{-1}.

Regarding the aged samples, a pronounced decrease of the surface area was observed only under the harsh hydrothermal treatment at 800 °C, since the γ-Al_2O_3 carrier was calcined for 5 h at 700 °C before the Pt deposition. The highest surface area after aging at 800°C was found for the FSP catalyst followed by the sample obtained via laser ablation. For the first case, the high thermal stability of carriers obtained by flame spray pyrolysis is well known[46-48]. The considerably higher surface area of the LA-800 sample can only be linked to morphological changes of the carrier during preparation, as already mentioned for the as prepared catalyst, which seem to lead to a higher thermal stability as compared to that shown by the commercial support.

Table 1: Pt content, specific surface area, mean pore diameter and total pore volume for calcined and aged samples at 800°C.

Catalyst		ICP-OES [wt.%]	S_{BET} [m^2g^{-1}]	Mean pore diameter [nm]	Total pore volume [cm^3g^{-1}]
HCP	500	1.9	165	12	0.51
	800		87	16	0.35
PAA	500	1.8	161	9	0.36
	800		90	15	0.34
FSP	500	2.2	220	41	2.25
	800		148	16	0.59
SC	500	2.3	167	12	0.50
	800		90	15	0.33
LA	500	1.2	183	10	0.48
	800		145	14	0.49

The results of the powder X-ray diffraction data collected for the fresh samples (calcined at 500°C) are given in Figure 1. The XRD patterns indicate the presence of γ-Al_2O_3 in all cases, with more broadened reflections for the FSP and LA catalysts.

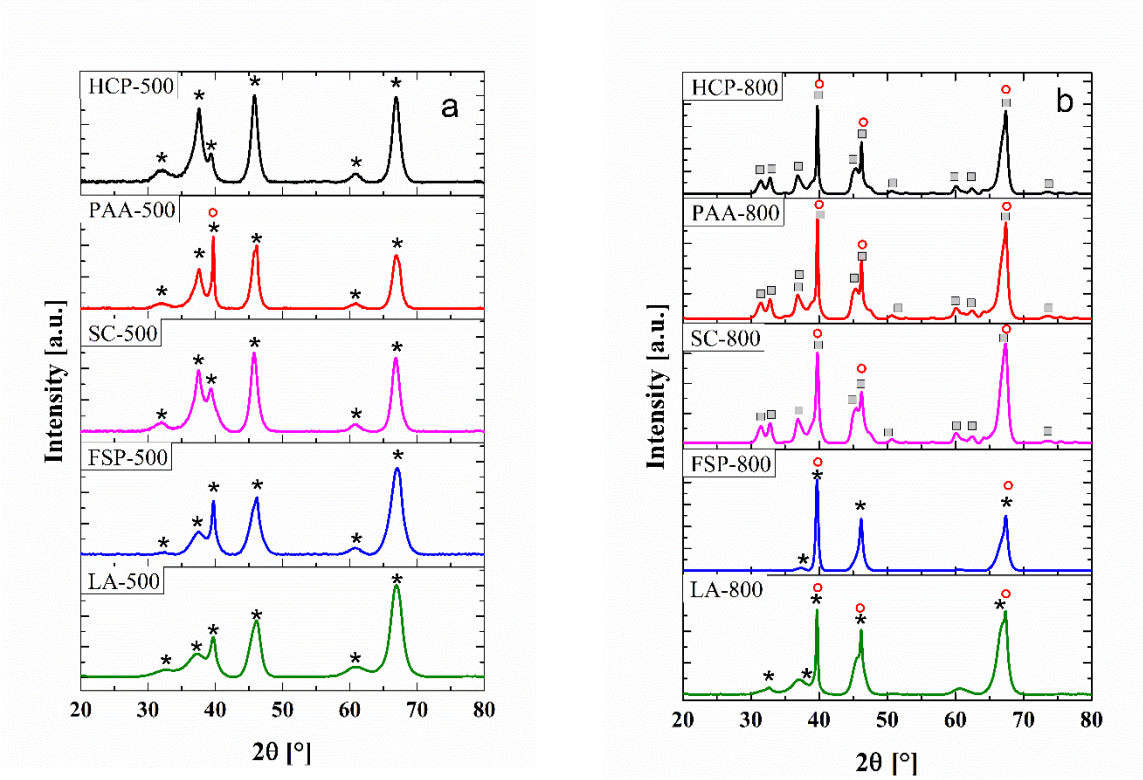

Figure 1: XRD patterns of a) calcined (500) and b) aged (800) samples with: * indicating diffraction peaks of γ-Al_2O_3, ° of metallic Pt and □ of θ-Al_2O_3.

The PAA-500 catalyst also shows clearly defined patterns corresponding to rather large metallic Pt particles. The absence of Pt reflections in all other catalysts is most probably due to the presence of very small Pt particles.

After the hydrothermal aging step at 800 °C the characteristic XRD patterns for metallic Pt were observed in all cases, indicating sintering of Pt particles. The distinct reflections observed at $2\theta = 40°$, $2\theta = 46°$ and $2\theta = 68°$ correspond well to the (111), (200) and (220) diffraction peaks of bulk fcc Pt. Finally, phase transformation of γ-Al_2O_3 to θ-modification was observed for the 800 °C thermally treated SC, PAA and HCP samples.

3.1.2 Pt oxidation state

Ex situ XAS measurements were performed for the fresh and hydrothermally aged catalysts in order to investigate the impact and the evolution of the oxidation state of platinum during aging. Figure 2 (a), (b), (c) shows the X-ray absorption near edge structure (XANES) spectra at the Pt L_3-edge. The intensity of the whiteline (the strong absorption feature just above the rising edge) unveils the vacant d band and is sensitive to the metal oxidation state[49]. An overview of the averaged oxidation state (obtained by using linear combination analysis (LCA) of the Pt L_3 XANES region) as a function of the aging temperature is reported in Table 2. The recorded spectra for the fresh samples (Figure 2 (a)) illustrate that the HCP-500 and FSP-500 samples contain mostly oxidized sites (~2+ average oxidation state) in comparison with the PAA-500 and SC-500 catalysts. The whiteline is the lowest for the LA-500 sample and an average oxidation state around 1+ was obtained by LCA of the XAS spectra. This is line with the presence of larger particles, most probably containing a reduced metallic core, as resulted upon laser ablation of the Pt metallic target.

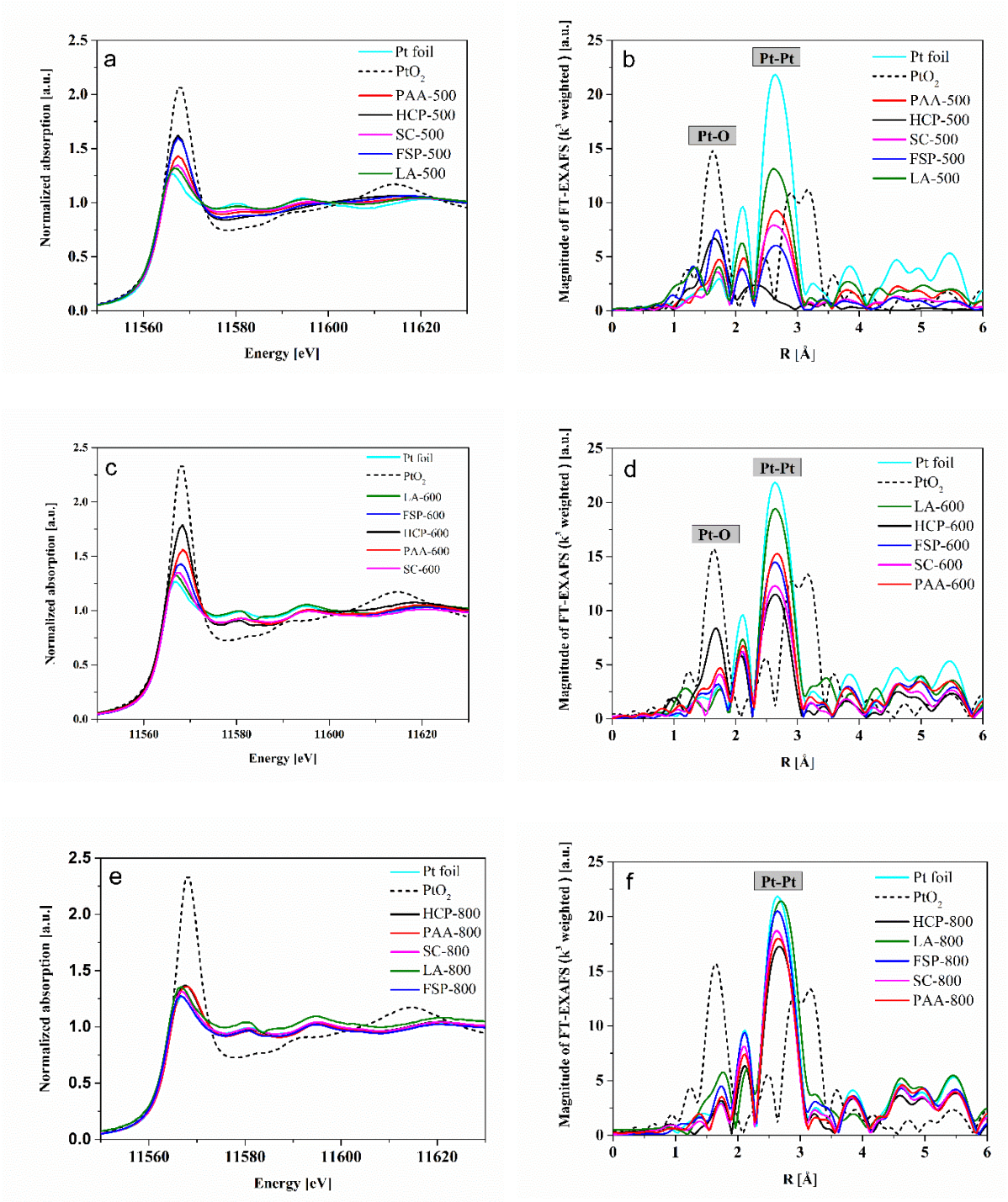

Figure 2: Pt L_3 XANES spectra of Pt/Al_2O_3 a) calcined catalysts and after hydrothermal aging at c) 600 °C and e) 800 °C, including the reference samples, and b), d), f) the corresponding k^3-weighted FT-EXAFS spectra.

After hydrothermal aging, a strong decrease of the oxidation state was observed for all samples, which is due to the decomposition of the oxidized Pt species[50]. The oxidation state variation is strongly influenced not only by the initial particle size but also by the preparation procedure. In

this regard, a clear trend is observed particularly after aging at 600°C, with the extent of oxidized Pt decreasing in the following order: HCP-600 > PAA-600 > FSP-600 > SC-600 > LA-600. The highest intensity of the whiteline was recorded for the HCP-600 sample, and corresponds still to a 2+ oxidation state. In contrast, the LA-600 catalyst showed the less pronounced whiteline, which corresponds to almost completely reduced Pt particles. After hydrothermal aging at 800 °C, all catalysts seem to contain mainly Pt^0 sites (Figure 2 c).

The corresponding Fourier transformed (FT) k^3-weighted EXAFS spectra are shown in the right column of Figure 2 (d) and (f) for the fresh and aged samples. Data fitting in R-space (Table 2) gives information about number and type of neighbors, interatomic distance and structural disorder. In comparison with the reference materials, bulk metallic Pt and PtO_2, among the fresh catalysts the HCP-500 has in the first shell mostly O neighbors with a characteristic distance of 2.01 Å. The FSP-500 shows backscattering not only from Pt-O, but also from Pt-Pt at a distance of 2.77 Å, which is typical for metallic Pt. For all other calcined samples the Pt-Pt backscattering dominates the FT-EXAFS spectra. In accordance with the XANES data, this confirms the presence of slightly larger and partially reduced noble metal nanoparticles in most of the fresh samples. Hence, once again the impact of the synthesis method on the noble metal particle size and oxidation state is clearly visible: the smallest Pt particles present in the HCP fresh catalyst and the largest in the LA sample correspond to the highest Pt-O and Pt-Pt coordination numbers (cf. section 3.2, Table 2), respectively.

As indicated by the FT-EXAFS spectra of the mildly aged catalysts, sintering of Pt particles occurs already at 600 °C. This is demonstrated by the intensity increase of the second coordination shell, which corresponds to the Pt-Pt scattering in metallic Pt, and by the decrease of the first Pt-O coordination shell. The most significant variations were observed for the HCP-600 and FSP-600 samples whereas for the catalyst prepared by SFRD only showed minor changes.

Finally, after hydrothermal aging at 800 °C predominantly contributions from the Pt-backscattering path characteristic for metallic Pt was found for the FSP-800, SC-800 and LA-800, which is consistent with full reduction of Pt particles. As it will be demonstrated in the following, although the XAS results represent an averaged structural state, the variations in oxidation tendency upon hydrothermal aging closely correlates with the respective increase of Pt particle size and catalytic activity.

Table 2: Summary of average Pt oxidation states and coordination environments determined from the XANES and EXAFS spectra

Catalyst*	Pt oxidation state	Pt-O distance [Å]	CN (O)	Pt-Pt distance [Å]	CN (Pt)	σ^2 [10^{-3} Å^2]	δE_0 [eV]	ρ [%]
HCP-500	2.14±0.01	2.01±0.02	3.2±0.5	2.62±0.02	1.4±1.2	3.4±1.7 (O) 6.6± 4.8(Pt)	14.1±1.7	1.9
HCP-600	1.92±0.03	1.98±0.01	2.0±0.5	2.76±0.008	8.3±2.0	-0.3±1.7 (O)* 6.0±1.1 (Pt)	9.1±1.7	2.5
HCP-800	0.66±0.01	1.99±0.13	0.6±0.8	2.76±0.009	11.5±2.9	5.7±1.2	7.4 ±2.3	5.9
PAA-500	1.36±0.02	1.995±0.01	1.8±0.3	2.77±0.007	4.9±0.9	3.2±2.5 (O) 4.7±0.8 (Pt)	11.9 ±1.4	1.4
PAA-600	1.24±0.05	1.97±0.02	1.7±0.6	2.76±0.006	9.4±1.4	3.5 ±4.6 (O) 5.2±0.7 (Pt)	8.3±1.3	1.5
PAA-800	0.54±0.02	1.96±0.03	0.7±0.2	2.76±0.004	11.2±0.9	5.2±0.4	7.2±0.8	0.5
FSP-500	2.06±0.02	2.01±0.02	2.6±0.6	2.78±0.02	3.6±1.9	1.8 ± 2.6 (O) 5.6±2.7 (Pt)	14.5 ± 2.4	3.0
FSP-600	0.83±0.02	1.96±0.02	1.3±0.2	2.76±0.005	9.2±0.9	5.3±0.5 (O) 5.3±0.5 (Pt)	7.2±1.0	0.8
FSP-800	0.12±0.04	-	-	2.76±0.003	10.7±0.8	4.4±0.3 (O) 4.4±0.3 (Pt)	6.9±0.7	0.3
SC-500	1.02±0.01	1.98±0.01	1.2±0.3	2.75±0.007	7.5±0.9	3.6 ±3.3 (O) 7.3±0.8 (Pt)	8.8±1.1	1.1
SC-600	0.54±0.01	2.00±0.03	1.0±0.3	2.76±0.006	8.4±1.0	5.4±0.5 (O) 5.4±0.5 (Pt)	8.2±1.4	1.1
SC-800	0.14±0.01	-	-	2.76±0.003	11.1±0.8	5.1±0.3 (Pt)	6.6±0.7	0.3
LA-500	0.87±0.04	-	-	2.75±0.01	9.0 ± 2.3	5.6 ±1.3 (Pt)	6.4 ± 2.2	2.3
LA-600	0.15±0.02	-	-	2.76±0.006	11.5±1.5	5.2±0.6 (Pt)	7.5±1.3	0.6
LA-800	0.06±0.03	-	-	2.78±0.011	12.9±3.8	5.5±1.1 (Pt)	9.0±2.6	2.4
Pt foil**	0	-	-	2.77±0.002	12	4.7±0.2 (Pt)	8.6±0.5	0.2
PtO_2 (ICSD 4415)	4	1.98 2.02 3.21	4 2 2	3.14 3,55	2 8	-	-	-

* The acronyms used in in the first column describe the preparation procedure and the calcination or aging temperature applied for each sample, e.g. "HCP-500" refers to the catalyst prepared by incipient wetness impregnation with hexachloroplatinic acid and calcined at 500°C, "HCP-600" represents the same sample aged at 600°C.
**Pt sites are possibly both bulk Pt and PtO_2 NPs. **Amplitude reduction factor (S^2_0) was determined from fitting a reference spectrum of bulk Pt (Pt foil) as 0.86 (PETRA, P64) and 0.79 (ANKA, CAT-ACT).

3.2 Initial Pt particle size distribution and impact of hydrothermal aging

The influence of the different preparation procedures on the PSD of Pt particles on γ-Al_2O_3 surface has been previously discussed in detail[14] and is only briefly described here. In general, the different preparation methods led to a good distribution of the noble metal component but variations in Pt particle size were encountered. The HAADF-STEM images of the fresh Pt/Al_2O_3 catalysts indicate the formation of a narrow particle size distribution for the catalysts prepared by incipient wetness impregnation with a Cl-containing precursor (mainly 1-2 nm, Figure 3a), supercritical fluid reactive deposition (mainly 2-4 nm, Figure 4a) and flame spray pyrolysis (2-3 nm, Figure S 1a). Homogeneous distribution but a combination of very small (diameters of 1-2 nm) and a few very large (diameters between 8 and 40 nm) Pt particles was observed if platinum (II) acetylacetonate was used as precursor during IWI (Figure S 2a). The only exception with a pronounced heterogeneous dispersion of Pt particles is the LA catalyst series, which shows a broader PSD (between 2 to 10 nm, with an averaged diameter of 3.4 nm, Figure S 3a). As discussed by Marzun et al.[37], the formation of larger particles typically occurs when a Gaussian beam profile is used during laser ablation and, thus, an uneven lateral laser distribution reaches the target. To narrow this distribution, oxidative laser-fragmentation has been shown to yield monodisperse, ligand-free noble metal particles with 2-3 nm diameter[29, 51], but has not been carried out here in order to allow better comparability with Pt particles generated in earlier PLAL studies. The HAADF-STEM images also indicate that the particle adsorption is not homogeneous or the particles adsorb preferentially on certain support sites (Fig. S 3d). To enable particle adsorption during LA, the pH value was set to ~3, between the isoelectric point (IEP) of the colloidal NPs and the support [30]. Since this pH value is near to the IEP of the Pt NPs, the particles' surface charge is low, that can lead to particle agglomeration, which then competes with the particle adsorption. Hence, most of the small nanoparticles appear to agglomerate at certain locations on the Al_2O_3 carrier. Accordingly, fine-tuning of the pH would

allow more homogeneous Pt NP dispersion during their adsorption on the alumina support, as has been demonstrated by Marzun et al. for titania catalyst supports[30].

Table 3: Mean particle diameter ($\mathbf{D_m}$) from STEM, surface particle diameter ($\mathbf{D_s}$) and dispersion of differently prepared and thermal treated Pt/Al_2O_3 catalysts.

Catalyst	$\mathbf{D_m}$ **STEM [nm]**	$\mathbf{D_s = \frac{\sum_i N_i D_i^3}{\sum_i N_i D_i^2}}$	$\mathbf{N_i}$
HCP-500	1.1	1.2	101
600	10.3	20.7	1682
700	10.2	20.5	1031
800	10.2	23.5	802
PAA-500	2.1	53.3*	124
600	20.1	75.5	324
700	21.0	69.5	518
800	63.2	83.4	182
FSP-500	1.8	2.65	1499
600	3.8	11.1	1782
700	5.4	29.4	299
800	7.7	26.5	296
SC-500	2.4	3.2	383
600	2.8	11.2	661
700	4.1	10	1623
800	8.0	27.8	299
LA-500	3.4	7.5	1054
600	8.8	13.6	636
700	24.2	51.7	631
800	42.6	100	301

A comparison of the mean Pt particle diameter ($\mathbf{D_m}$), directly obtained from HAADF STEM images, and the calculated surface-averaged Pt particle size ($\mathbf{D_s}$)[5] is provided in Table 3, assuming spherical particle shape for all catalysts. It can be observed that these two sizes are similar for the fresh samples. Only in the case of the impregnated PAA-500 sample a variation between the D_m and D_s values was observed. This is due to several very large Pt particles present in this catalyst, which have a major effect on the D_s value (D_m = 2.1 nm vs. D_s = 53 nm).

Summing up, the fresh catalysts prepared by the different methods belong to different classes regarding size, size distribution and surface dispersion of the noble metal components, which is expected to affect the sintering process and the corresponding catalyst activity.

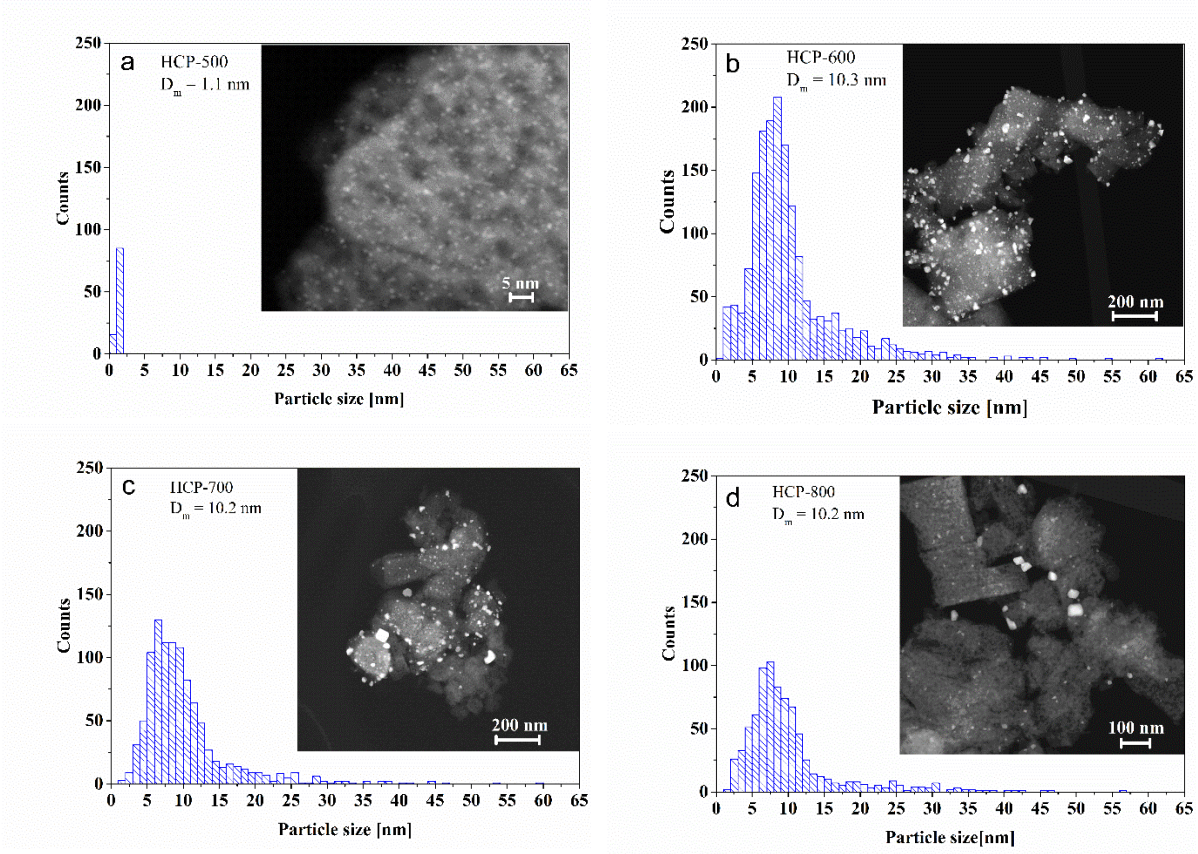

Figure 3: HAADF-STEM images of the HCP catalyst with corresponding particle size distribution histograms after various thermal treatments: a) HCP-500, b) HCP-600, c) HCP-700 and d) HCP-800. The number of particles analyzed to obtain the particle size distribution was 101 for HCP-500, 1682 for HCP-600, 1031 for HCP-700, and 802 for HCP-800 catalysts.

The sintering of the noble metal particles is illustrated for all catalysts by the increase of their average D_m and D_s values with the aging temperature (Table 3). Generally, for the aged samples D_s is always larger than D_m even if larger particles are not so numerous. However, they are dominantly weighted when compared to many small particles. From the STEM images (Figure 3b, Figure 4b, Figure S 2 and Figure S 3) it is observed that hydrothermal aging for 5 h at 600°C leads to a marked increase of Pt particle size in most of the samples.

For the HCP catalyst, which contains nanoparticles smaller than 2 nm, the mean particle size increases from 1.1 to 10.3 nm, with a maximum of the PSD profile between 7-10 nm and a tail up to 65 nm (Figure 3). A similar trend was observed for the PAA-600 sample but in this case most of the resulting Pt particles have sizes ranging between 3-6 nm (Figure S 2b).

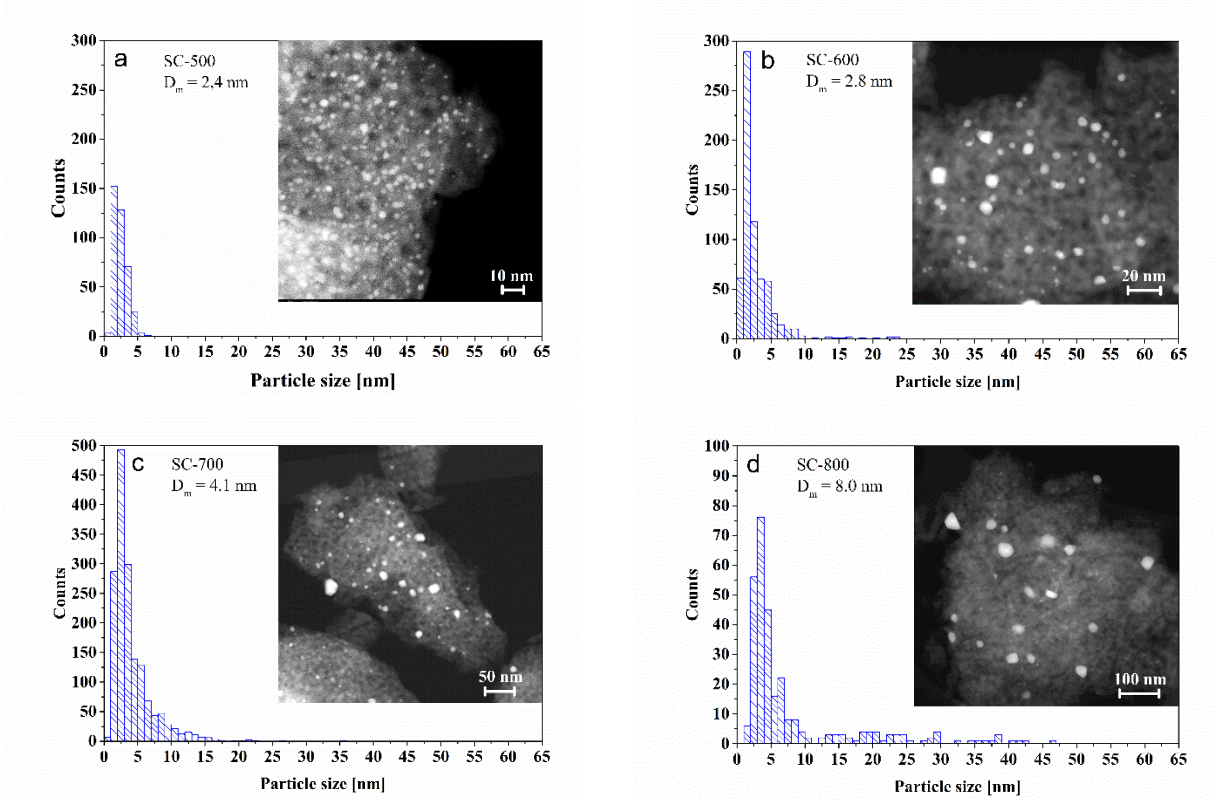

Figure 4: HAADF-STEM images of the catalyst obtained by SFRD with corresponding histograms of particle size distribution after different thermal treatments: a) SC-500, b) SC-600, c) SC-700, d) SC-800. Number of particles analyzed to obtain particle size distribution was 383 for SC-500, 661 for SC-600, 1623 for SC-700 and 299 for SC-800 catalysts.

This behavior confirms the high sintering rate of very small nanoparticles with a small curvature radius due to the tremendous increase of the chemical potential with the decrease of NP size, as previously[52] demonstrated for Pb atoms on MgO (100), for Au/TiO_2[18] and recently also for a Pd based three-way catalyst[19]. For such small particles Ostwald ripening and interparticle transport is often claimed[17], even in the absence of a pronounced tail towards smaller nanoparticles in the PSD profile[20]. According to the DFT simulation results of Plessow et al.[21], sintering

via the PtO_2 vapor phase under oxidizing conditions is highly promoted for an initial PSD centered at lower D_m values[21]. This is the case for the HCP and PAA catalysts, which contain mostly oxidized Pt nanoparticles (Figure 2). Additionally, in this temperature range the sintering process seems to be promoted by the chlorine traces, which are probably present in the HCP-500 catalyst. According to previous studies[53-54], chlorine remains after catalyst calcination in a dry atmosphere and is very slowly eliminated during catalyst operation in the presence of water.

Interestingly the FSP-600 sample, which in fresh state contains Pt particles with a D_m of 1.8 nm in combination with a higher BET surface area (220 m^2 vs. 165 m^2), prevents substantial sintering at 600 °C (Figure S 1). This behavior points to a stronger impact of the carrier morphology, surface area and resulting interaction with the noble metal[55-56] in comparison to the expected high diffusivity of the very small Pt nanoparticles in the FSP-500 catalyst (Figures S4 and 5A), effect which is maintained also at higher temperatures. Hence, upon aging at 600°C, the FSP-600 sample contains a very large number of small Pt nanoparticles alongside with larger Pt particles with diameters about 5-15 nm, resulting in a well-defined bimodal particle size distribution. Such a bimodal PSD has been linked to a transient stage of the sintering process[22], irrespective of the sintering mechanism, i.e. OR or PMC[20].

The SC catalyst, with Pt nanoparticle sizes in the fresh state mostly between 2-4 nm, is only slightly affected by the hydrothermal aging at 600 °C. This is in agreement with the significantly lower diffusivity of the slightly larger nanoparticles ($1/radius^4$ dependence[57], Figure S 4), e.g. in comparison with the HCP-500 sample. In this case the D_m increases from 2.4 nm to 2.8 nm and only a few larger particles, up to 25 nm, in size were observed (Figure 4b). This is in line with the previous studies in the literature[23], which reported a limited mobility of slightly larger nanoparticles. For the catalyst prepared by laser ablation, an almost synchronous increase of the noble metal particles was observed, with a D_m variation after aging from 3.4 nm to 8.8 nm

and a particle size distribution varying mainly from 1-10 nm to 4-20 nm, respectively (Figure S 3b). Such a behavior could be due to the close vicinity of Pt NPs[56], caused by their inhomogeneous dispersion on the support. All in all, according to the evolution of D_m (Figure 5) and D_s values for Pt/Al_2O_3 samples, hydrothermal aging at 600 °C uncovers a rapid sintering for the HCP, PAA and LA catalysts. This behavior corresponds to the fast disappearance of the small NPs, which is according to Hansen et al.[17] related to a first rapid stage of sintering. In contrast, a higher sintering stability was observed for the SC and FSP catalysts within this temperature range, both having an initial narrow PSD combined but slightly larger Pt NPs or deposited on a higher surface area support, respectively.

Hydrothermal aging at 700 °C only leads to a slight variation of the mean particle diameter Dm for all investigated catalysts, excepting the LA Pt/Al_2O_3 sample (Figure 5). This could be explained either by the limited migration of larger Pt nanoparticles or negligible inter-particle transfer (increase of the inter-particle distance as compared to the fresh catalyst) combined with a relatively thermally stable support (conditioned before impregnation at 700 °C). However, it is important to note that the ratio between the number of Pt NPs with $D_i < 5$ nm and the number of larger particles is decreasing for all studied samples, indicating the continuation of the sintering process. For the catalyst prepared by LA, once again the more localized distribution of Pt NPs (interparticle distance < 1 nm) has most probably contributed to the significant increase of Pt particle size, from a D_m of 8.8 nm to 24.3 nm. This assumption is supported by the study of Behafarid and Cuenya[56] on the sintering behavior of Au nanoparticles supported on TiC films.

An additional temperature increase to 800 °C leads to a considerable decrease of the Pt dispersion for all catalysts due to the sintering of the noble metal particles associated with alumina sintering. About 40-50 % decrease of the BET surface area was measured for the HCP, PAA and SC catalysts (Table 1). However, the Pt particle size variation strongly differs for the three

samples, with a D_m increasing in the order SC < HCP < PAA (Table 3). On the one side the impact of the initial particle size and sample homogeneity is obvious, even at such high temperatures (Figure 5). The sample obtained by SFRD, with Pt NP sizes of about 2-4 nm in the fresh state, suffers from sintering and Pt particles of up to 50 nm in diameters were identified in the HAADF-STEM images. Nonetheless, smaller NPs (D_i < 5 nm) could be still observed. Even if a longer aging time would lead to the complete disappearance of such small particles, the deceleration of the sintering process by preparing catalysts with slightly larger noble metal nanoparticles is worth to be considered. For the HCP catalyst virtually no change in the particle size distribution compared to the sample aged at 700°C could be observed (Figure 3). Most probably some chlorine traces remaining from the chloroplatinic acid precursor even after 5h hydrothermal aging inhibit the further particle growth, as the previously reported reverse process of Pt redispersion by oxychlorination[58-59] could balance the sintering. In comparison, although the fresh PAA sample contained very small Pt NPs, hydrothermal aging at 800 °C led to strong sintering, and only large Pt particles (10-140 nm) were detected by HAADF-STEM (Figure S 2d). The samples prepared by flame spray pyrolysis and laser ablation showed a superior thermal resistance of the alumina support, the BET surface area decreased upon aging by only 30% and 20 %, respectively (Table 1). This has a positive impact on the FSP catalyst, as a D_m around 7.7 nm was determined for the sample aged at 800 °C (Figure S 1d). In this case, the presence of small Pt NPs along with larger particles contributed to the relatively low D_m value.

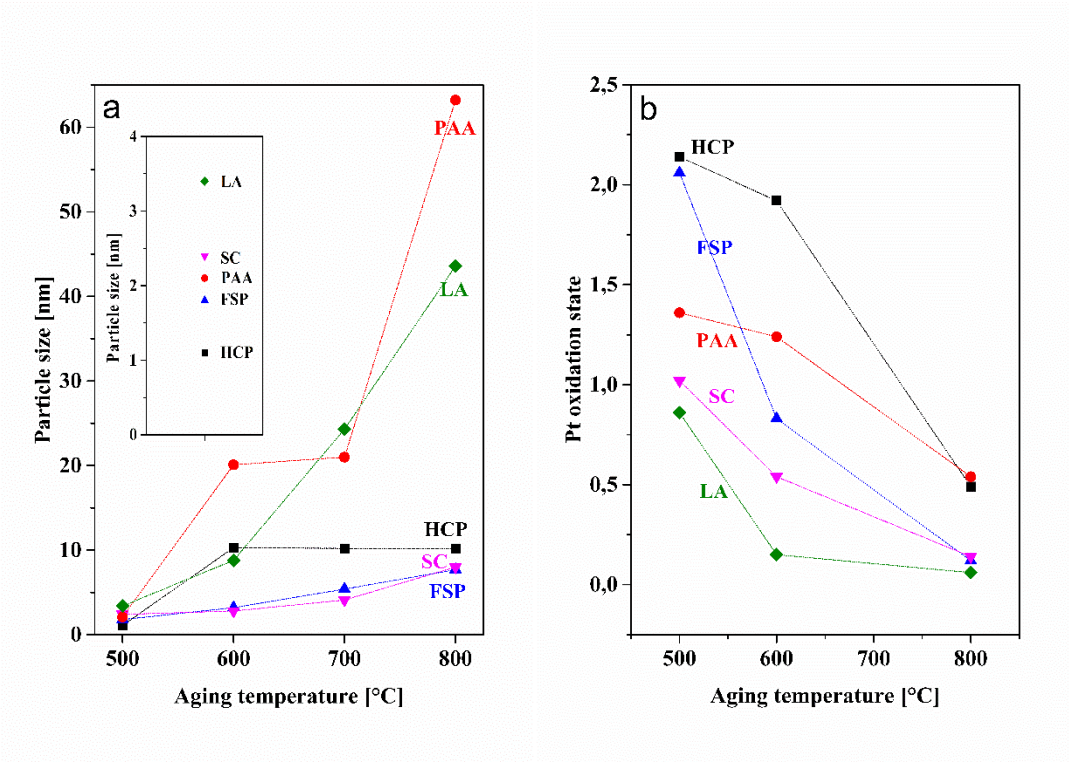

Figure 5: Variation of a) the mean particle sizes (D_m) and b) Pt oxidation state for the different catalysts during aging treatments with zoomed starting point of mean particle sizes. (note: PSD of the LA sample ignoring the big agglomerates). Dotted lines serve only as guides to the eye.

For the LA-800 catalyst the PSD profile changes significantly as compared to the catalyst aged at 700 °C (D_m variation from 24.3 to 43.6 nm), and no predominant size (very broad PSD) could be identified (Figure S 3d). Assumingly, if laser generated NPs would be adsorbed more homogeneously on the alumina, a comparable high catalyst stability as the FSP sample could be attained.

Summarizing the hydrothermal aging results (Figure 5), a rapid sintering already occurs at 600 °C especially for the catalysts containing very small Pt NPs (D_i < 2 nm in Figure 5a). This leads simultaneously to partial reduction of Pt sites (Figure 5b). As observed for the HCP catalyst, the possible presence of chlorine traces [53-54] might prevent a stronger sintering. A pronounced increase of the noble metal nanoparticles could be also restrained if slightly larger (D_i ~ 2-4 nm) and homogeneously distributed Pt particles are formed during preparation of the Pt/Al_2O_3 catalyst, i.e. either by SFRD or if an alumina support with higher thermal stability is

used, for example obtained by flame spray pyrolysis. Heterogeneous or more localized deposition of the noble metal component leads to rapid and massive sintering of the noble metal particles, as here illustrated for the sample prepared by pulsed laser ablation.

3.3 Correlations with catalytic performance in CO- and NO-oxidation

3.3.1 Hydrothermal aging impact on CO oxidation activity of Pt/Al_2O_3 catalysts

The conversion profiles for CO oxidation are shown in Figure 6 for the as-prepared (solid lines) and aged at 800 °C (dashed lines) catalysts. The CO oxidation light-offs upon aging at 600 °C and 700 °C are reported in the SI (Figure S 5) and the T_{50} values in the summary Figure 7.

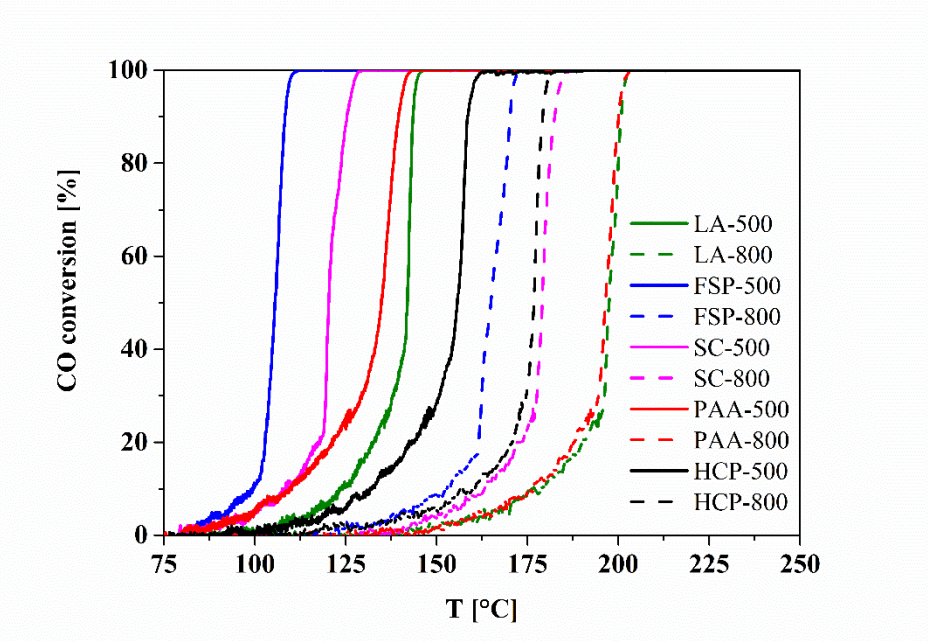

Figure 6: CO oxidation light-off of 3rd cycle over differently prepared calcined (solid lines) and aged at 800 °C (dashed lines) Pt/Al_2O_3 catalysts. Gas mixture: 500 ml/min of 1000 ppm CO, 10 % O_2, N_2 with heating rate 5 °C min^{-1}, measured between 50-350 °C.

The CO oxidation performance of the fresh catalysts increases in the order HCP < LA < PAA < SC < FSP. This is in line with the previously reported optimal Pt particle size of about 2-3 nm

for CO oxidation, which is present in the catalysts prepared by flame spray pyrolysis and supercritical fluid reactive deposition[14 16]. According to Gänzler et al.[11], slightly larger particles are easier reduced, generating the active metallic state during CO oxidation. Additionally, such particles are less poisoned by CO at low temperatures[14]. Hence, the highest T_{50} temperature was recorded for the Pt/Al_2O_3 HCP catalyst, which contains Pt NPs with a mean diameter of 1.1 nm and mainly oxidized Pt^{2+} site. Similarly, the fresh Pt/Al_2O_3 PAA catalyst also exhibits a lower CO conversion activity due to the large number of very small and oxidized Pt NPs. For the catalyst prepared by laser ablation, two effects contribute to the low CO oxidation activity: the presence of oxidized Pt NPs < 2 nm and the decrease of the available surface active sites for the larger Pt particles, as also indicated by the D_s value in Table 3.

Hydrothermal aging at 600 °C leads to a significant shift of the light-off temperature for most of the investigated samples, resulting in the T_{50} order of LA-600 < FSP-600 ≤ SC-600 << HCP-600 < PAA-600. Considering the sintering behavior presented previously, this confirms the sensitivity of CO oxidation to the number of active sites and noble metal oxidation state in the low-temperature range, where the CO poisoning is predominant. Thus, an increase of about 25 °C for T_{50} was measured for the HCP-600 and SC-600 samples. The similar T_{50} variation, although in one of the cases only a slight increase of D_m was observed (2.4 vs 2.8 nm), should be interpreted also considering the formation of much larger nanoparticles (up to 25 nm) in the SC-600 sample, which substantially decreases the number of surface active sites (increase of the volume-surface mean diameter D_s from 3.2 to 11.2 nm) and affects the low-temperature CO oxidation activity. In addition to the strong sintering of Pt particles in the HCP-600 but also in the PAA-600 sample, the presence of more oxidized Pt sites in both samples (Figure 5b) could contribute as well to the low performance of these catalysts. At the same time, 50 % CO conversion was achieved for the FSP-600 catalyst at about 40 °C higher temperature. Analogous to the SC-600 sample, the shift of the CO oxidation activity for the FSP-600 catalyst should be

related to the formation of larger Pt nanoparticles in addition to the very small ones (< 5 nm, D_s increase from 2.7 to 11.1 nm). Only the LA-600 shows almost the same light-off temperature in comparison to the corresponding fresh sample, which could be due to the small variation of the D_s combined with the more localized CO oxidation exothermicity, around adjacent Pt particles. The last aspect is also suggested by the slightly steeper light-off curve of the fresh and LA-600 Pt/Al_2O_3 samples (Figure 6 and Figure S 5). All in all, it results that the mild hydrothermal aging at 600 °C significantly influences the noble metal particle size and oxidation state and consequently the CO oxidation activity of alumina supported Pt catalysts. However, in all cases the fingerprint of the preparation procedure and initial performance is still visible, with the catalysts less prone to severe sintering showing the best performance upon aging.

As presented in the previous section, hydrothermal aging at 700 °C does not further affect the D_m or D_s of Pt NPs for the HCP-700 and PAA-700 samples, which have already undergone a major drop of noble metal dispersion during aging at 600°C. This is also visible in the slight variation (only about 5 °C, Figure S 5) of the T_{50} for the two catalysts. For all other samples, an additional increase of about 15-20 °C was measured for the light-off temperature. This is due to the further rise of the ratio between large and small particles. Nevertheless, also upon hydrothermal aging at 700 °C, the fingerprint of the initial activity is maintained, except the catalyst prepared by laser ablation: LA-700 ≤ FSP-700 ≤ SC-700 < HCP-700 <PAA-700.

The more severe hydrothermal aging at 800 °C led to only 5-10 °C additional shift of the light-off temperature for the PAA-800, FSP-800 and SC-800 catalysts. In contrast, a 40 °C higher T_{50} was measured for the LA-800 as compared to the LA-700, due to the considerable increase of the Pt particle size. Hydrothermal aging at such high temperatures demonstrates that the final impact on the long-term stability of CO oxidation activity is given by a high thermally stable catalyst carrier, in this study obtained by flame spray pyrolysis. The FSP catalyst shows the

lowest light-off temperature after hydrothermal aging for 5 h at 800 °C. Additional stabilization factors are the possible presence of chlorine traces after the relatively short hydrothermal aging step (HCP Pt/Al_2O_3 catalyst) or the preparation of a catalyst with homogeneously distributed slightly larger Pt nanoparticles, about 2-3 nm in size (e.g. by SFRD).

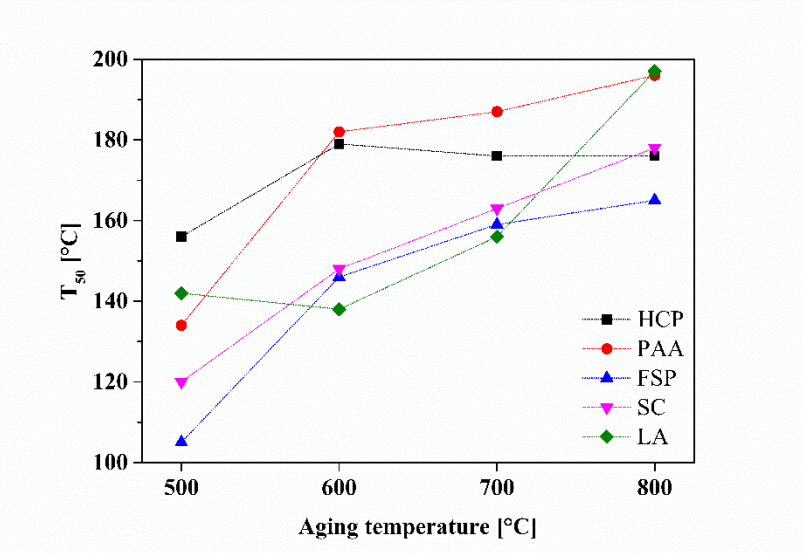

Figure 7: Light-off temperatures of the 3rd CO oxidation cycle as a function of aging temperatures for the differently prepared Pt/Al_2O_3 catalysts. Dotted lines serve only as guides to the eye.

3.3.2 Hydrothermal aging impact on NO oxidation activity of Pt/Al_2O_3 catalysts

The trends of NO oxidation for the fresh catalysts indicate the highest performance for the LA catalyst (D_m of 3.8 nm), with about 82 % NO oxidation activity at 290 °C (Figure 8a). The maximum conversion decreases following the order LA-500 >> FSP-500 ≥ SC-500 > PAA-500 >> HCP-500. In general, this is in line with previous studies which reported a lower conversion for catalysts containing very small Pt NPs[5]. According to Boubnov et al.[5] NO oxidation is facilitated over reduced surface Pt sites on planar facets that are present in larger nanoparticles. This observation is clearly confirmed by the variation in activity reported here for the fresh catalysts, with the most active sample, i.e. LA-500 catalyst, containing larger Pt particles and the lowest oxidation state (around 1+). On the contrary, NO oxidation is marginal (about 30 %

at 410 °C) for the HCP-500 sample that comprises very small and completely oxidized nanoparticles. Furthermore, in contrast to the CO oxidation activity, sintering of nanoparticles by mild hydrothermal aging at 600 °C leads to an increase of performance and shift of the maximum NO conversion towards lower temperatures for the FSP-600, SC-600, PAA-600 and HCP-600 samples. Due to virtually the same number of exposed Pt surface sites (D_s values in Table 3) for the SC-600 and FSP-600 samples, both catalysts convert about 75 % NO at 300 °C. Nearly 20 % conversion enhancement was measured for the HCP-600 catalyst whereas only 5 % was measured for the PAA-600 sample. Solely the catalyst prepared by pulse laser ablation loses about 25 % NO oxidation activity upon noble metal particle sintering (Figure 8b).

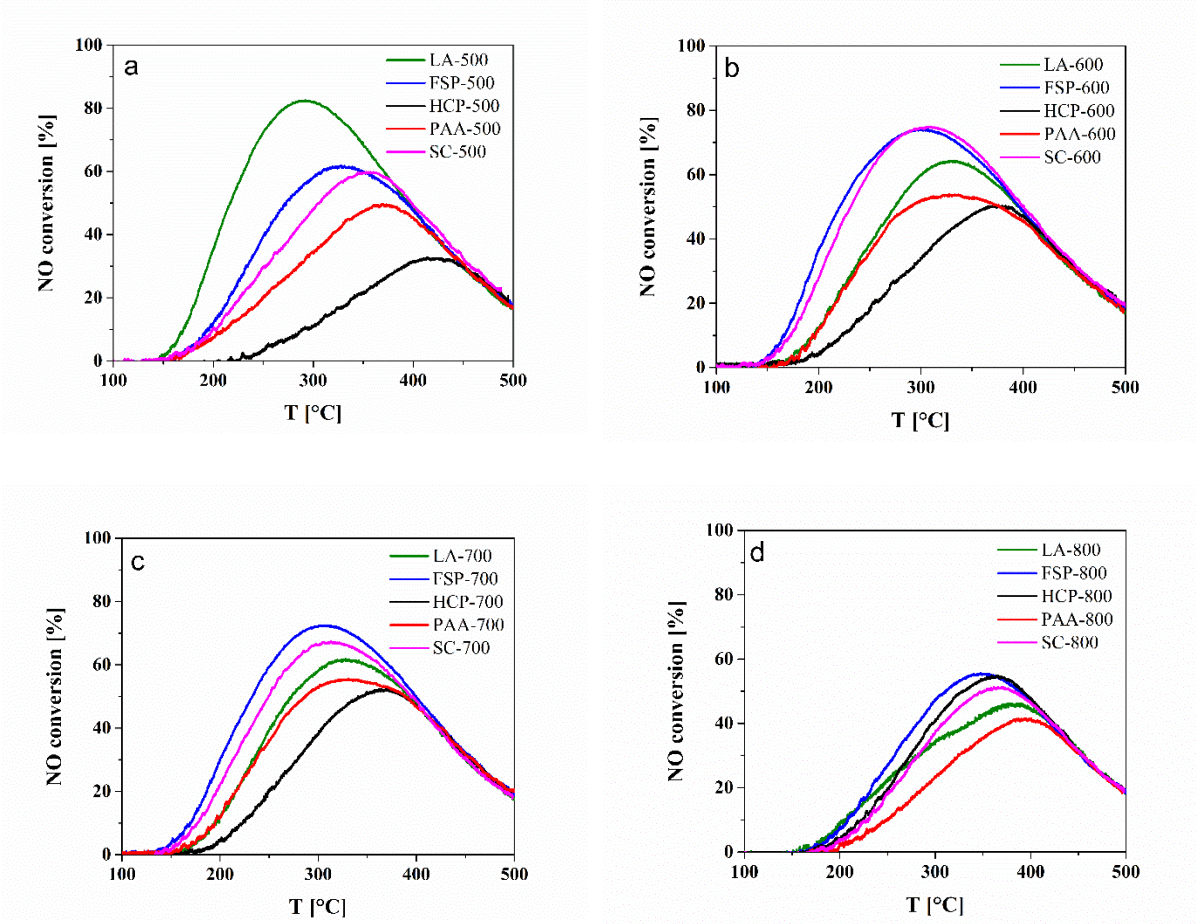

Figure 8: NO conversion curves over differently prepared catalysts a) after calcination at 500 °C, after hydrothermal aging at b) 600 °C, c) 700 °C and d) 800 °C. Reaction conditions: 1000 ppm CO, 10 vol.% O_2 in N_2 at a total flow of 500 mL min^{-1}.

Similar to the relatively small variation in CO oxidation activity, further increase of the hydrothermal aging temperature to 700 °C only leads to minor changes in performance for all investigated catalysts (Figure 8c). The FSP-700, PAA-700 and the HCP-700 even show no variation of the NO oxidation activity under the applied testing conditions of this study. A slight decrease in NO conversion is only shown by the catalyst prepared by SFRD and by the LA-700 sample (< 10 % in maximum conversion).

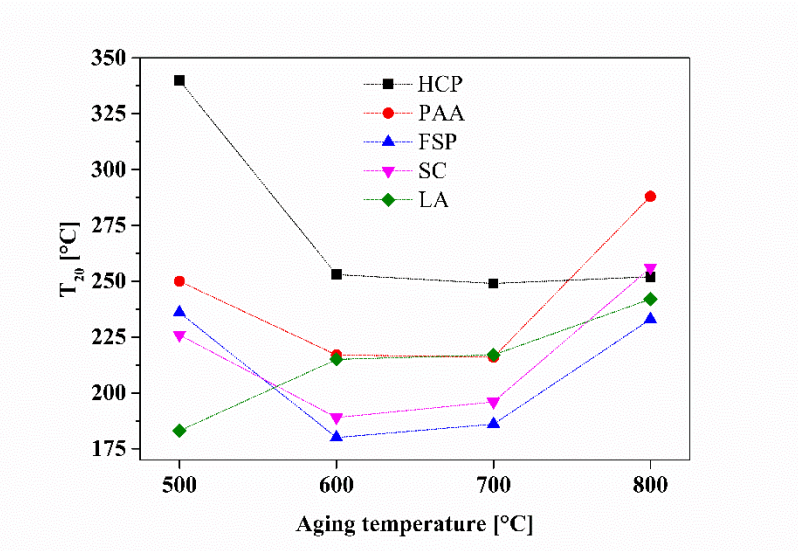

Figure 9: T_{20} (20 % NO conversion) versus aging temperatures of all studied catalysts. Gas mixture: 500 mL min^{-1} of 1000 ppm NO, 10 % O_2, N_2 with heating rate 5 °C min^{-1}, measured between 50-500 °C. Dotted lines serve only as guides to the eye.

As expected, the pronounced sintering of the noble metal particles and of the alumina support at 800 °C strongly affects the NO_x conversion of all studied Pt/Al_2O_3 catalysts. A decrease of about 17 % was measured for the SC-800 in comparison to the same sample aged at 700 °C (Figure 8d). Only the catalyst prepared by impregnation with a Cl-containing precursor seems to not be affected, which is in agreement with the observed stability of the noble metal particles in this sample. An almost identical NO oxidation ability (~55 %) at a slightly lower temperature (350 °C vs. 360 °C) is also maintained for the catalyst prepared by flame spray pyrolysis, due to the higher thermal stability of such materials[60].

The summary of the results on the hydrothermal aging impact on the NO conversion of the differently prepared Pt/Al_2O_3 catalysts is presented in Figure 9 by the T_{20} temperature evolution (temperature of 20 % conversion) as a function of the aging temperature. Considering the variation of Pt dispersion during aging, an optimal particle size of about 3-4 nm and a narrow particle size distribution seems to be optimal for high NO conversion. As clarified by previous studies[5], slightly larger nanoparticles containing reduced Pt terrace atoms are more resistant towards surface oxidation, and facilitate the NO conversion. This hypothesis is supported by the XANES results presented in Figure 2, which show a significant reduction of Pt sites during particle growth. Furthermore, the promotion of the NO conversion in the presence of a reductant, e.g. CO, underlines that the NO to NO_2 oxidation mechanism involves reduced Pt nanoparticles [5].

4 Conclusions

In the present study the impact of the preparation method and of the resulting particle size distribution on the behavior during hydrothermal aging and the corresponding CO and NO oxidation activity of $Pt/\gamma\text{-}Al_2O_3$ catalysts has been systematically investigated. By careful selecting representative conventional and modern preparation methods, the following conclusions can be drawn:

- Significant differences in the size and distribution of Pt particles were identified for conventional and advanced preparation methods, also depending on the noble metal precursor.
- Three different categories of Pt/Al_2O_3 catalysts were obtained: (i) catalysts containing homogeneously distributed Pt nanoparticles with $D_i < 2$ nm, prepared with chlorine-containing precursor; (ii) catalysts with homogeneously distributed but slightly larger Pt nanoparticles with $D_i \sim 2\text{-}4$ nm, prepared by supercritical fluid reactive deposition and flame spray pyrolysis; (iii) heterogeneous particle size distribution containing either a combination of small

and large Pt particles (platinum(II) acetylacetonate precursor) or insufficient distribution of the noble metal component (pulse laser ablation).

- The fastest sintering behavior resulting in the formation of very large Pt particles (e.g. D_m of 65 nm for PAA-800 catalyst) was observed for the catalysts containing oxidized Pt NPs smaller than 2 nm. In this case, the presence of chlorine traces from Pt precursor could stabilize further sintering of the noble metal particles (D_m ~10 nm after aging at 600 °C, which remains constant after the 800 °C aging of the HCP catalyst).
- The preparation of catalysts with slightly larger Pt nanoparticles (e.g. obtained by super-critical fluid reactive deposition) is suitable to significantly decelerate the sintering process at mild aging temperatures (< 800 °C). In addition, modern preparation methods like super-critical fluid reactive deposition and flame spray pyrolysis should be further considered in future.
- The increased thermal stability of the alumina carrier also positively impacts the sintering process. In this regard, the samples prepared by flame spray pyrolysis and laser ablation showed superior thermal resistance of the support.
- The variation of the CO and NO oxidation activity for the fresh and hydrothermally aged samples is closely related to the changes in Pt dispersion and oxidation state during aging. The results support the presence of reduced Pt sites as mandatory prerequisite for both processes, as uncovered by the XAS measurements.
- The optimal particle size of about 2-3 nm was confirmed for the CO oxidation reaction whereas slightly larger Pt particles with diameters of 3-4 nm lead to the highest NO conversion at lower temperatures.

Although the study requires further investigations under more realistic conditions or similar aging investigations of typical bimetallic Pt-Pd DOC catalysts, the obtained results help in understanding the impact of the preparation method on the resulting hydrothermal aging behavior,

which should allow to develop more sintering resistant catalysts. In addition to the initial noble metal particle size and distribution on the support surface, the noble metal oxidation state, precursor traces and carrier morphology were identified as essential parameters determining progress of catalyst aging and resulting activity. Furthermore, the use of CO and NO oxidation is suitable as test reactions to gain complementary information on the noble metal particle size distribution.

Supporting Information Available: Additional characterization data as figures and table.

Acknowledgements

We thank Dr. Thomas Bergfeldt, Institute for Applied Materials- Applied Materials Physics (IAM-AWP, KIT) for elemental analysis. Marlene Crone (Institute for Technical Thermodynamics and Refrigeration, ITTK) is acknowledged for preparation of SC-CO_2 samples and Angela Beilmann (ITCP, KIT) for conducting BET analysis. We further thank KIT for financial support. GM, CM and SB acknowledge the German Federal Ministry of Education and Research (BMBF) for the financial support within the INNOKAT project (FKZ 03X5523). German Research Foundation (DFG) is acknowledged for the financial support with the project INST 121384/70-1.

References

1. *Catalyst Preparation: Science and Engineering*; Regalbuto, J., Ed.; CRC Press: Boca Raton, 2016.
2. Regalbuto, J.; Navada, A.; Shadid, S.; Bricker, M.; Chen, Q., An Experimental Verification of the Physical Nature of Pt Adsorption onto Alumina. *J. Catal.* **1999**, *184*, 335-348.
3. Cho, H.-R.; Regalbuto, J. R., The Rational Synthesis of Pt-Pd Bimetallic Catalysts by Electrostatic Adsorption. *Catal. Today* **2015**, *246*, 143-153.
4. Kang, J. H.; Menard, L. D.; Nuzzo, R. G.; Frenkel, A. I., Unusual Non-Bulk Properties in Nanoscale Materials: Thermal Metal-Metal Bond Contraction of γ-Alumina-Supported Pt Catalysts. *J. Am. Chem. Soc.* **2006**, *128*, 12068-12069.
5. Boubnov, A.; Dahl, S.; Johnson, E.; Molina, A. P.; Simonsen, S. B.; Cano, F. M.; Helveg, S.; Lemus-Yegres, L. J.; Grunwaldt, J.-D., Structure–Activity Relationships of Pt/Al_2O_3 Catalysts for CO and NO Oxidation at Diesel Exhaust Conditions. *Appl. Catal. B* **2012**, *126*, 315-325.
6. Gracia, F. J.; Bollmann, L.; Wolf, E. E.; Miller, J. T.; Kropf, A. J., In Situ Ftir, Exafs, and Activity Studies of the Effect of Crystallite Size on Silica-Supported Pt Oxidation Catalysts. *J. Catal.* **2003**, *220*, 382-391.
7. Smeltz, A. D.; Delgass, W. N.; Ribeiro, F. H., Oxidation of No with O2 on Pt(111) and Pt(321) Large Single Crystals. *Langmuir* **2010**, *26*, 16578-16588.
8. Heiz, U.; Sanchez, A.; Abbet, S.; Schneider, W. D., Catalytic Oxidation of Carbon Monoxide on Monodispersed Platinum Clusters: Each Atom Counts. *J. Am. Chem. Soc.* **1999**, *121*, 3214-3217.
9. Doronkin, D. E.; Kuriganova, A. B.; Leontyev, I. N.; Baier, S.; Lichtenberg, H.; Smirnova, N. V.; Grunwaldt, J.-D., Electrochemically Synthesized Pt/Al_2O_3 Oxidation Catalysts. *Catal. Lett.* **2016**, *146*, 452-463.
10. Roldan Cuenya, B.; Behafarid, F., Nanocatalysis: Size- and Shape-Dependent Chemisorption and Catalytic Reactivity. *Surf. Sci. Rep.* **2015**, *70*, 135-187.
11. Gänzler, A. M.; Casapu, M.; Boubnov, A.; Müller, O.; Conrad, S.; Lichtenberg, H.; Frahm, R.; Grunwaldt, J.-D., Operando Spatially and Time-Resolved X-Ray Absorption Spectroscopy and Infrared Thermography During Oscillatory CO Oxidation. *J. Catal.* **2015**, *328*, 216-224.
12. Hansen, T. K.; Høj, M.; Hansen, B. B.; Janssens, T. V. W.; Jensen, A. D., The Effect of Pt Particle Size on the Oxidation of CO, C_3H_6, and NO over Pt/Al_2O_3 for Diesel Exhaust Aftertreatment. *Top. Catal.* **2017**, *60*, 1333-1344.
13. Lira, E.; Merte, L.; Behafarid, F.; Ono, L.; Zhang, L.; Roldan Cuenya, B., Role and Evolution of Nanoparticle Structure and Chemical State During the Oxidation of NO over Size- and Shape-Controlled $Pt/\gamma\text{-}Al_2O_3$ Catalysts under Operando Conditions. *ACS Catal.* **2014**, *4*, 1875-1884.
14. Casapu, M.; Fischer, A.; Gänzler, A. M.; Popescu, R.; Crone, M.; Gerthsen, D.; Türk, M.; Grunwaldt, J.-D., Origin of the Normal and Inverse Hysteresis Behavior During CO Oxidation over Pt/Al_2O_3. *ACS Catal.* **2017**, *7*, 343-355.
15. Gänzler, A. M.; Casapu, M.; Vernoux, P.; Loridant, S.; Cadete Santos Aires, F. J.; Epicier, T.; Betz, B.; Hoyer, R.; Grunwaldt, J.-D., Tuning the Structure of Platinum Particles on Ceria in Situ for Enhancing the Catalytic Performance of Exhaust Gas Catalysts. *Angew. Chem.* **2017**, *129*, 13258-13262.
16. Boubnov, A.; Gänzler, A.; Conrad, S.; Casapu, M.; Grunwaldt, J.-D., Oscillatory CO Oxidation over Pt/Al_2O_3 Catalysts Studied by in Situ XAS and DRIFTS. *Top. Catal.* **2013**, *56*, 333-338.

17. Hansen, T. W.; DeLaRiva, A. T.; Challa, S. R.; Datye, A. K., Sintering of Catalytic Nanoparticles: Particle Migration or Ostwald Ripening? *Acc. Chem. Res.* **2013**, *46*, 1720-1730.
18. Campbell, C. T.; Parker, S. C.; Starr, D. E., The Effect of Size-Dependent Nanoparticle Energetics on Catalyst Sintering. *Science* **2002**, *298*, 811-814.
19. Kang, S. B.; Lim, J. B.; Jo, D.; Nam, I.-S.; Cho, B. K.; Hong, S. B.; Kim, C. H.; Oh, S. H., Ostwald-Ripening Sintering Kinetics of Pd-Based Three-Way Catalyst: Importance of Initial Particle Size of Pd. *Chem. Eng. J.* **2017**, *316*, 631-644.
20. Datye, A. K.; Xu, Q.; Kharas, K. C.; McCarty, J. M., Particle Size Distributions in Heterogeneous Catalysts: What Do They Tell Us About the Sintering Mechanism? *Catal. Today* **2006**, *111*, 59-67.
21. Plessow, P. N.; Abild-Pedersen, F., Sintering of Pt Nanoparticles Via Volatile PtO_2: Simulation and Comparison with Experiments. *ACS Catal.* **2016**, *6*, 7098-7108.
22. Tabib Zadeh Adibi, P.; Zhdanov, V. P.; Langhammer, C.; Grönbeck, H., Transient Bimodal Particle Size Distributions During Pt Sintering on Alumina and Silica. *J. Phys. Chem. C* **2015**, *119*, 989-996.
23. Simonsen, S. B.; Chorkendorff, I.; Dahl, S.; Skoglundh, M.; Sehested, J.; Helveg, S., Direct Observations of Oxygen-Induced Platinum Nanoparticle Ripening Studied by in Situ Tem. *J. Am. Chem. Soc.* **2010**, *132*, 7968-7975.
24. Russell, A.; Epling, W. S., Diesel Oxidation Catalysts. *Catal. Rev.* **2011**, *53*, 337-423.
25. Strobel, R.; Pratsinis, S. E., Flame Aerosol Synthesis of Smart Nanostructured Materials. *J. Mater. Chem.* **2007**, *17*, 4743-4756.
26. Türk, M., *Particle Formation with Supercritical Fluids: Challenges and Limitations*; Kiran, E., Ed.; Elsevier: Amsterdam, 2014; Vol. 6.
27. Erkey, C., *Supercritical Fluids and Organometallic Compounds: From Recovery of Trace Metals to Synthesis of Nanostructured Materials;* Kiran, E., Ed.; Elsevier: Amsterdam, 2011; Vol. 1.
28. Fischer, M.; Hormes, J.; Marzun, G.; Wagener, P.; Hagemann, U.; Barcikowski, S., In Situ Investigations of Laser-Generated Ligand-Free Platinum Nanoparticles by X-Ray Absorption Spectroscopy: How Does the Immediate Environment Influence the Particle Surface? *Langmuir* **2016**, *32*, 8793-8802.
29. Zhang, D.; Gökce, B.; Barcikowski, S., Laser Synthesis and Processing of Colloids: Fundamentals and Applications. *Chemical reviews* **2017**, *117*, 3990-4103.
30. Marzun, G.; Streich, C.; Jendrzej, S.; Barcikowski, S.; Wagener, P., Adsorption of Colloidal Platinum Nanoparticles to Supports: Charge Transfer and Effects of Electrostatic and Steric Interactions. *Langmuir* **2014**, *30*, 11928-11936.
31. Tepluchin, M.; Casapu, M.; Boubnov, A.; Lichtenberg, H.; Wang, D.; Kureti, S.; Grunwaldt, J.-D., Fe and Mn-Based Catalysts Supported on γ-Al_2O_3 for CO Oxidation under O_2-Rich Conditions. *ChemCatChem* **2014**, *6*, 1763-1773.
32. Teoh, W. Y.; Amal, R.; Madler, L., Flame Spray Pyrolysis: An Enabling Technology for Nanoparticles Design and Fabrication. *Nanoscale* **2010**, *2*, 1324-1347.
33. Garrido, G. I.; Patcas, F. C.; Upper, G.; Türk, M.; Yilmaz, S.; Kraushaar-Czarnetzki, B., Supercritical Deposition of Pt on SnO_2-Coated Al_2O_3 Foams: Phase Behaviour and Catalytic Performance. *Appl. Cat. A* **2008**, *338*, 58-65.
34. Wolff, S.; Crone, M.; Muller, T.; Enders, M.; Bräse, S.; Türk, M., Preparation of Supported Pt Nanoparticles by Supercritical Fluid Reactive Deposition: Influence of Precursor, Substrate and Pressure on Product Properties. *J. Supercrit. Fluids* **2014**, *95*, 588-596.
35. Lang, S.; Türk, M.; Kraushaar-Czarnetzki, B., Novel $PtCuO/CeO_2/\alpha$-Al_2O_3 Sponge Catalysts for the Preferential Oxidation of CO (PROX) Prepared by Means of Supercritical Fluid Reactive Deposition (SFRD). *J. Catal.* **2012**, *286*, 78-87.
36. Türk, M.; Erkey, C., Synthesis of supported nano particles in supercritical fluids by supercritical fluid reactive deposition: Current state, further perspectives and needs, *J.*

Supercrit. Fluids **2018**, *134*, 176–183 .
37. Marzun, G.; Nakamura, J.; Zhang, X.; Barcikowski, S.; Wagener, P., Size Control and Supporting of Palladium Nanoparticles Made by Laser Ablation in Saline Solution as a Facile Route to Heterogeneous Catalysts. *Appl. Surf. Sci.* **2015**, *348*, 75-84.
38. Drube, W.; Bieler, M.; Caliebe, W. A.; Schulte-Schrepping, H.; Spengler, J.; Tischer, M.; Wanzenberg, R., The Petra III Extension. *AIP Conf. Proc.* **2016**, *1741*, 020035.
39. Zimina, A., et al., CAT-AACT - a New Highly Versatile X-Ray Spectroscopy Beamline for Catalysis and Radionuclide Science at the KIT Synchrotron Light Facility ANKA. *Rev. Sci. Instrum.* **2017**, *88*, 113113.
40. Ravel, B.; Newville, M., Athena, Artemis, Hephaestus: Data Analysis for X-Ray Absorption Spectroscopy Using Ifeffit. *J. Synchrotron Radiat.* **2005**, *12*, 537-541.
41. Abràmoff, M. D.; Magalhães, P. J.; Ram, S. J., Image Processing with ImageJ. *Biophotonics Int.* **2004**, *11*, 36-42.
42. Bergeret, G.; Gallezot, P., Particle Size and Dispersion Measurements. In *Handbook of Heterogeneous Catalysis*, Wiley-VCH Verlag GmbH & Co. KGaA: 2008.
43. Roelofs, F.; Vogelsberger, W., Dissolution Kinetics of Nanodispersed Γ-Alumina in Aqueous Solution at Different Ph: Unusual Kinetic Size Effect and Formation of a New Phase. *J. Colloid Interface Sci.* **2006**, *303*, 450-459.
44. Roelofs, F.; Vogelsberger, W.; Buntkowsky, G., Kinetic Size Effect During Dissolution of a Synthetic γ-Alumina. *Z. Phys. Chem.* **2008**, *222*, 1131-1153.
45. Strobel, R.; Krumeich, F.; Stark, W. J.; Pratsinis, S. E.; Baiker, A., Flame Spray Synthesis of Pd/Al_2O_3 Catalysts and Their Behavior in Enantioselective Hydrogenation. *J. Catal.* **2004**, *222*, 307-314.
46. Strobel, R.; Pratsinis, S. E.; Baiker, A., Flame-Made $Pd/La_2O_3/Al_2O_3$ Nanoparticles: Thermal Stability and Catalytic Behavior in Methane Combustion. *J. Mater. Chem.* **2005**, *15*, 605-610.
47. Mädler, L.; Stark, W. J.; Pratsinis, S. E., Flame-Made Ceria Nanoparticles. *J. Mater. Res.* **2002**, *17*, 1356-1362.
48. Stark, W. J.; Maciejewski, M.; Mädler, L.; Pratsinis, S. E.; Baiker, A., Flame-Made Nanocrystalline Ceria/Zirconia: Structural Properties and Dynamic Oxygen Exchange Capacity. *J. Catal.* **2003**, *220*, 35-43.
49. Singh, J.; Lamberti, C.; van Bokhoven, J. A., Advanced X-Ray Absorption and Emission Spectroscopy: In Situ Catalytic Studies. *Chem. Soc. Rev.* **2010**, *39*, 4754-4766.
50. Ono, L. K.; Croy, J. R.; Heinrich, H.; Roldan Cuenya, B., Oxygen Chemisorption, Formation, and Thermal Stability of Pt Oxides on Pt Nanoparticles Supported on SiO_2/Si(001): Size Effects. *J. Phys. Chem. C* **2011**, *115*, 16856-16866.
51. Lau, M.; Haxhiaj, I.; Wagener, P.; Intartaglia, R.; Brandi, F.; Nakamura, J.; Barcikowski, S., Ligand-Free Gold Atom Clusters Adsorbed on Graphene Nano Sheets Generated by Oxidative Laser Fragmentation in Water. *Chem. Phys. Lett.* **2014**, *610*, 256-260.
52. Starr, D. E.; Bald, D. J.; Musgrove, J. E.; Ranney, J. T.; Campbell, C. T., Microcalorimetric Measurements of the Heat of Adsorption of Pb on Well-Defined Oxides: MgO(100) and P(2×1)-Oxide on Mo(100). *J. Chem. Phys.* **2001**, *114*, 3752-3764.
53. Gélin, P.; Primet, M., Complete Oxidation of Methane at Low Temperature over Noble Metal Based Catalysts: A Review. *Appl. Catal. B* **2002**, *39*, 1-37.
54. Marceau, E.; Che, M.; Saint-Just, J.; Tatibouët, J., Influence of Chlorine Ions in $Pt/A1_2O_3$ Catalysts for Methane Total Oxidation. *Catal. Today* **1996**, *29*, 415-419.
55. Campbell, C. T., The Energetics of Supported Metal Nanoparticles: Relationships to Sintering Rates and Catalytic Activity. *Acc. Chem. Res.* **2013**, *46*, 1712-1719.
56. Behafarid, F.; Roldan Cuenya, B., Towards the Understanding of Sintering Phenomena at the Nanoscale: Geometric and Environmental Effects. *Top. Catal.* **2013**, *56*, 1542-1559.

57. Jak, M. J., An Atomic Scale View on a Model Catalyst: Pd Nanoparticles on TiO_2. Ph.D. Dissertation, Universiteit Leiden, Leiden, NL, 2000.
58. Morgan, K.; Goguet, A.; Hardacre, C., Metal Redispersion Strategies for Recycling of Supported Metal Catalysts: A Perspective. *ACS Catal.* **2015**, *5*, 3430-3445.
59. Neyestanaki, A. K.; Klingstedt, F.; Salmi, T.; Murzin, D. Y., Deactivation of Postcombustion Catalysts, a Review. *Fuel* **2004**, *83*, 395-408.
60. Strobel, R.; Baiker, A.; Pratsinis, S., Aerosol Flame Synthesis of Catalysts. *Adv. Powder Technol.* **2006**, *17*, 457-480..

TOC Graphic

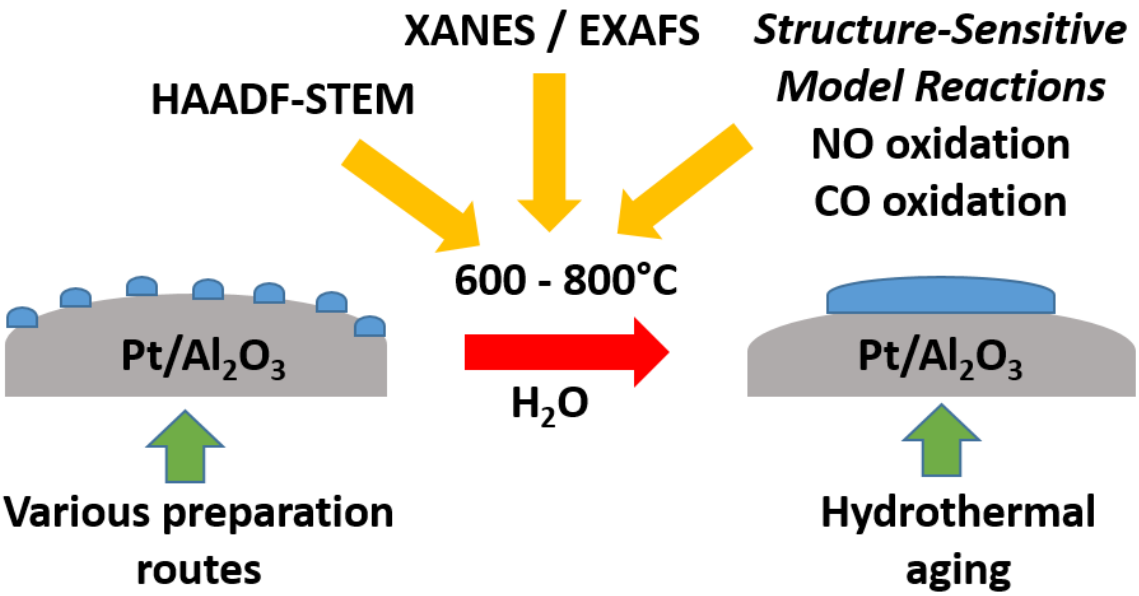
XANES / EXAFS
HAADF-STEM
Structure-Sensitive
Model Reactions
NO oxidation
CO oxidation
600 - 800°C
Pt/Al2O3
H2O
Pt/Al2O3
Various preparation
routes
Hydrothermal
aging